Old Dominion University

ODU Digital Commons

Physics Faculty Publications

Physics

2020

Results on Total and Elastic Cross Sections in Proton−Proton Collisions at √s = 200 GeV

J. Adam

L. Adamczyk

J. R. Adams

S. Bueltmann
Old Dominion University, sbueltma@odu.edu

Z. Zhu

See next page for additional authors

Follow this and additional works at: https://digitalcommons.odu.edu/physics_fac_pubs

Part of the Nuclear Commons

Authors

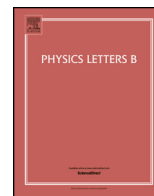J. Adam, L. Adamczyk, J. R. Adams, S. Bueltmann, Z. Zhu, M. Zyzak, Et al., and STAR Collaboration

Results on total and elastic cross sections in proton–proton collisions at $\sqrt{s} = 200$ GeV

STAR Collaboration

J. Adam [f], L. Adamczyk [b], J.R. Adams [am], J.K. Adkins [ad], G. Agakishiev [ab], M.M. Aggarwal [ap], Z. Ahammed [bj], I. Alekseev [c,ai], D.M. Anderson [bd], A. Aparin [ab], E.C. Aschenauer [f], M.U. Ashraf [k], F.G. Atetalla [ac], A. Attri [ap], G.S. Averichev [ab], V. Bairathi [bb], K. Barish [j], A. Behera [ba], R. Bellwied [t], A. Bhasin [aa], J. Bielcik [n], J. Bielcikova [al], L.C. Bland [f], I.G. Bordyuzhin [c], J.D. Brandenburg [f,ax], A.V. Brandin [ai], S. Bueltmann [an], J. Butterworth [at], H. Caines [bm], M. Calderón de la Barca Sánchez [h], D. Cebra [h], I. Chakaberia [ac,f], P. Chaloupka [n], B.K. Chan [i], F-H. Chang [ak], Z. Chang [f], N. Chankova-Bunzarova [ab], A. Chatterjee [k], D. Chen [j], J.H. Chen [r], X. Chen [aw], Z. Chen [ax], J. Cheng [bf], M. Cherney [m], M. Chevalier [j], S. Choudhury [r], W. Christie [f], X. Chu [f], H.J. Crawford [g], M. Csanád [p], M. Daugherity [a], T.G. Dedovich [ab], I.M. Deppner [s], A.A. Derevschikov [ar], L. Didenko [f], X. Dong [ae], J.L. Drachenberg [a], J.C. Dunlop [f], T. Edmonds [as], N. Elsey [bl], J. Engelage [g], G. Eppley [at], S. Esumi [bg], O. Evdokimov [l], A. Ewigleben [af], O. Eyser [f], R. Fatemi [ad], S. Fazio [f], P. Federic [al], J. Fedorisin [ab], C.J. Feng [ak], Y. Feng [as], P. Filip [ab], E. Finch [az], Y. Fisyak [f], A. Francisco [bm], L. Fulek [b], C.A. Gagliardi [bd], T. Galatyuk [o], F. Geurts [at], A. Gibson [bi], K. Gopal [w], D. Grosnick [bi], W. Guryn [f,*], A.I. Hamad [ac], A. Hamed [e], S. Harabasz [o], J.W. Harris [bm], S. He [k], W. He [r], X.H. He [z], S. Heppelmann [h], S. Heppelmann [aq], N. Herrmann [s], E. Hoffman [t], L. Holub [n], Y. Hong [ae], Y. Horvat [bm], Y. Hu [r], H.Z. Huang [i], S.L. Huang [ba], T. Huang [ak], X. Huang [bf], T.J. Humanic [am], P. Huo [ba], G. Igo [i], D. Isenhower [a], W.W. Jacobs [y], C. Jena [w], A. Jentsch [f], Y. Ji [aw], J. Jia [f,ba], K. Jiang [aw], S. Jowzaee [bl], X. Ju [aw], E.G. Judd [g], S. Kabana [bb], M.L. Kabir [j], S. Kagamaster [af], D. Kalinkin [y], K. Kang [bf], D. Kapukchyan [j], K. Kauder [f], H.W. Ke [f], D. Keane [ac], A. Kechechyan [ab], M. Kelsey [ae], Y.V. Khyzhniak [ai], D.P. Kikoła [bk], C. Kim [j], B. Kimelman [h], D. Kincses [p], T.A. Kinghorn [h], I. Kisel [q], A. Kiselev [f], M. Kocan [n], L. Kochenda [ai], L.K. Kosarzewski [n], L. Kramarik [n], P. Kravtsov [ai], K. Krueger [d], N. Kulathunga Mudiyanselage [t], L. Kumar [ap], S. Kumar [z], R. Kunnawalkam Elayavalli [bl], J.H. Kwasizur [y], R. Lacey [ba], S. Lan [k], J.M. Landgraf [f], J. Lauret [f], A. Lebedev [f], R. Lednicky [ab], J.H. Lee [f], Y.H. Leung [ae], C. Li [aw], W. Li [ay], W. Li [at], X. Li [aw], Y. Li [bf], Y. Liang [ac], R. Licenik [al], T. Lin [bd], Y. Lin [k], M.A. Lisa [am], F. Liu [k], H. Liu [y], P. Liu [ba], P. Liu [ay], T. Liu [bm], X. Liu [am], Y. Liu [bd], Z. Liu [aw], T. Ljubicic [f], W.J. Llope [bl], R.S. Longacre [f], N.S. Lukow [bc], S. Luo [l], X. Luo [k], G.L. Ma [ay], L. Ma [r], R. Ma [f], Y.G. Ma [ay], N. Magdy [l], R. Majka [bm], D. Mallick [aj], S. Margetis [ac], C. Markert [be], H.S. Matis [ae], J.A. Mazer [au], N.G. Minaev [ar], S. Mioduszewski [bd], B. Mohanty [aj], I. Mooney [bl], Z. Moravcova [n], D.A. Morozov [ar], M. Nagy [p], J.D. Nam [bc], Md. Nasim [v], K. Nayak [k], D. Neff [i], J.M. Nelson [g], D.B. Nemes [bm], M. Nie [ax], G. Nigmatkulov [ai], T. Niida [bg], L.V. Nogach [ar], T. Nonaka [bg], A.S. Nunes [f], G. Odyniec [ae], A. Ogawa [f], S. Oh [ae], V.A. Okorokov [ai], B.S. Page [f], R. Pak [f],

A. Pandav [aj], Y. Panebratsev [ab], B. Pawlik [ao], D. Pawlowska [bk], H. Pei [k], C. Perkins [g],
L. Pinsky [t], R.L. Pintér [p], J. Pluta [bk], J. Porter [ae], M. Posik [bc], N.K. Pruthi [ap], M. Przybycien [b],
J. Putschke [bl], H. Qiu [z], A. Quintero [bc], S.K. Radhakrishnan [ac], S. Ramachandran [ad],
R.L. Ray [be], R. Reed [af], H.G. Ritter [ae], O.V. Rogachevskiy [ab], J.L. Romero [h], L. Ruan [f],
J. Rusnak [al], N.R. Sahoo [ax], H. Sako [bg], S. Salur [au], J. Sandweiss [bm], S. Sato [bg], W.B. Schmidke [f],
N. Schmitz [ag], B.R. Schweid [ba], F. Seck [o], J. Seger [m], M. Sergeeva [i], R. Seto [j], P. Seyboth [ag],
N. Shah [x], E. Shahaliev [ab], P.V. Shanmuganathan [f], M. Shao [aw], A.I. Sheikh [ac], F. Shen [ax],
W.Q. Shen [ay], S.S. Shi [k], Q.Y. Shou [ay], E.P. Sichtermann [ae], R. Sikora [b], M. Simko [al], J. Singh [ap],
S. Singha [z], N. Smirnov [bm], W. Solyst [y], P. Sorensen [f], H.M. Spinka [d], B. Srivastava [as],
T.D.S. Stanislaus [bi], M. Stefaniak [bk], D.J. Stewart [bm], M. Strikhanov [ai], B. Stringfellow [as],
A.A.P. Suaide [av], M. Sumbera [al], B. Summa [aq], X.M. Sun [k], X. Sun [l], Y. Sun [aw], Y. Sun [u],
B. Surrow [bc], D.N. Svirida [c], P. Szymanski [bk], A.H. Tang [f], Z. Tang [aw], A. Taranenko [ai],
T. Tarnowsky [ah], J.H. Thomas [ae], A.R. Timmins [t], D. Tlusty [m], M. Tokarev [ab], C.A. Tomkiel [af],
S. Trentalange [i], R.E. Tribble [bd], P. Tribedy [f], S.K. Tripathy [p], O.D. Tsai [i], Z. Tu [f], T. Ullrich [f],
D.G. Underwood [d], I. Upsal [ax,f], G. Van Buren [f], J. Vanek [al], A.N. Vasiliev [ar], I. Vassiliev [q],
F. Videbæk [f], S. Vokal [ab], S.A. Voloshin [bl], F. Wang [as], G. Wang [i], J.S. Wang [u], P. Wang [aw],
Y. Wang [k], Y. Wang [bf], Z. Wang [ax], J.C. Webb [f], P.C. Weidenkaff [s], L. Wen [i], G.D. Westfall [ah],
H. Wieman [ae], S.W. Wissink [y], R. Witt [bh], Y. Wu [j], Z.G. Xiao [bf], G. Xie [ae], W. Xie [as], H. Xu [u],
N. Xu [ae], Q.H. Xu [ax], Y.F. Xu [ay], Y. Xu [ax], Z. Xu [f], Z. Xu [i], C. Yang [ax], Q. Yang [ax], S. Yang [f],
Y. Yang [ak], Z. Yang [k], Z. Ye [at], Z. Ye [l], L. Yi [ax], K. Yip [f], H. Zbroszczyk [bk], W. Zha [aw], C. Zhang [ba],
D. Zhang [k], S. Zhang [aw], S. Zhang [ay], X.P. Zhang [bf], Y. Zhang [aw], Y. Zhang [k], Z.J. Zhang [ak],
Z. Zhang [f], Z. Zhang [l], J. Zhao [as], C. Zhong [ay], C. Zhou [ay], X. Zhu [bf], Z. Zhu [ax], M. Zurek [ae],
M. Zyzak [q]

a *Abilene Christian University, Abilene, TX 79699*
b *AGH University of Science and Technology, FPACS, Cracow 30-059, Poland*
c *Alikhanov Institute for Theoretical and Experimental Physics NRC "Kurchatov Institute", Moscow 117218, Russia*
d *Argonne National Laboratory, Argonne, IL 60439*
e *American University of Cairo, New Cairo 11835, New Cairo, Egypt*
f *Brookhaven National Laboratory, Upton, NY 11973*
g *University of California, Berkeley, CA 94720*
h *University of California, Davis, CA 95616*
i *University of California, Los Angeles, CA 90095*
j *University of California, Riverside, CA 92521*
k *Central China Normal University, Wuhan, Hubei 430079*
l *University of Illinois at Chicago, Chicago, IL 60607*
m *Creighton University, Omaha, NE 68178*
n *Czech Technical University in Prague, FNSPE, Prague 115 19, Czech Republic*
o *Technische Universität Darmstadt, Darmstadt 64289, Germany*
p *ELTE Eötvös Loránd University, Budapest, H-1117 Hungary*
q *Frankfurt Institute for Advanced Studies FIAS, Frankfurt 60438, Germany*
r *Fudan University, Shanghai, 200433*
s *University of Heidelberg, Heidelberg 69120, Germany*
t *University of Houston, Houston, TX 77204*
u *Huzhou University, Huzhou, Zhejiang 313000*
v *Indian Institute of Science Education and Research (IISER), Berhampur 760010, India*
w *Indian Institute of Science Education and Research (IISER) Tirupati, Tirupati 517507, India*
x *Indian Institute Technology, Patna, Bihar 801106, India*
y *Indiana University, Bloomington, IN 47408*
z *Institute of Modern Physics, Chinese Academy of Sciences, Lanzhou, Gansu 730000*
aa *University of Jammu, Jammu 180001, India*
ab *Joint Institute for Nuclear Research, Dubna 141 980, Russia*
ac *Kent State University, Kent, OH 44242*
ad *University of Kentucky, Lexington, KY 40506-0055*
ae *Lawrence Berkeley National Laboratory, Berkeley, CA 94720*
af *Lehigh University, Bethlehem, PA 18015*
ag *Max-Planck-Institut für Physik, Munich 80805, Germany*
ah *Michigan State University, East Lansing, MI 48824*
ai *National Research Nuclear University MEPhI, Moscow 115409, Russia*
aj *National Institute of Science Education and Research, HBNI, Jatni 752050, India*
ak *National Cheng Kung University, Tainan 70101*
al *Nuclear Physics Institute of the CAS, Rez 250 68, Czech Republic*
am *Ohio State University, Columbus, OH 43210*
an *Old Dominion University, Norfolk, VA 23529*
ao *Institute of Nuclear Physics PAN, Cracow 31-342, Poland*
ap *Panjab University, Chandigarh 160014, India*
aq *Pennsylvania State University, University Park, PA 16802*
ar *NRC "Kurchatov Institute", Institute of High Energy Physics, Protvino 142281, Russia*
as *Purdue University, West Lafayette, IN 47907*

[at] *Rice University, Houston, TX 77251*
[au] *Rutgers University, Piscataway, NJ 08854*
[av] *Universidade de São Paulo, São Paulo, 05314-970, Brazil*
[aw] *University of Science and Technology of China, Hefei, Anhui 230026*
[ax] *Shandong University, Qingdao, Shandong 266237*
[ay] *Shanghai Institute of Applied Physics, Chinese Academy of Sciences, Shanghai 201800*
[az] *Southern Connecticut State University, New Haven, CT 06515*
[ba] *State University of New York, Stony Brook, NY 11794*
[bb] *Instituto de Alta Investigación, Universidad de Tarapacá, Arica 1000000, Chile*
[bc] *Temple University, Philadelphia, PA 19122*
[bd] *Texas A&M University, College Station, TX 77843*
[be] *University of Texas, Austin, TX 78712*
[bf] *Tsinghua University, Beijing 100084*
[bg] *University of Tsukuba, Tsukuba, Ibaraki 305-8571, Japan*
[bh] *United States Naval Academy, Annapolis, MD 21402*
[bi] *Valparaiso University, Valparaiso, IN 46383*
[bj] *Variable Energy Cyclotron Centre, Kolkata 700064, India*
[bk] *Warsaw University of Technology, Warsaw 00-661, Poland*
[bl] *Wayne State University, Detroit, MI 48201*
[bm] *Yale University, New Haven, CT 06520*

A R T I C L E   I N F O

A B S T R A C T

We report results on the total and elastic cross sections in proton-proton collisions at $\sqrt{s} = 200$ GeV obtained with the Roman Pot setup of the STAR experiment at the Relativistic Heavy Ion Collider (RHIC). The elastic differential cross section was measured in the squared four-momentum transfer range $0.045 \leq -t \leq 0.135$ GeV^2. The value of the exponential slope parameter B of the elastic differential cross section $d\sigma/dt \sim e^{-Bt}$ in the measured $-t$ range was found to be $B = 14.32 \pm 0.09(stat.)^{+0.13}_{-0.28}(syst.)$ GeV^{-2}. The total cross section σ_{tot}, obtained from extrapolation of the $d\sigma/dt$ to the optical point at $-t = 0$, is $\sigma_{tot} = 54.67 \pm 0.21(stat.)^{+1.28}_{-1.38}(syst.)$ mb. We also present the values of the elastic cross section $\sigma_{el} = 10.85 \pm 0.03(stat.)^{+0.49}_{-0.41}(syst.)$ mb, the elastic cross section integrated within the STAR t-range $\sigma_{el}^{det} = 4.05 \pm 0.01(stat.)^{+0.18}_{-0.17}(syst.)$ mb, and the inelastic cross section $\sigma_{inel} = 43.82 \pm 0.21(stat.)^{+1.37}_{-1.44}(syst.)$ mb. The results are compared with the world data.

1. Introduction

Elastic scattering plays an important role in proton-proton (pp) scattering at high energies, as evidenced by the fact that it contributes about 20% of the total cross section at the highest Large Hadron Collider (LHC) energies [1]. The pp elastic and total cross sections have been measured at colliders with center of mass energies $2.76 \leq \sqrt{s} \leq 13$ TeV at the LHC [1] and at the Intersecting Storage Rings (ISR) at $\sqrt{s} = 62.4$ GeV [2]. It is important, however, to have measurements in the energy gap between the ISR and the LHC to constrain the phenomenological models of the pp cross sections since one still expects a difference between pp and proton-antiproton ($p\bar{p}$) cross sections within the RHIC energy range. The latter were measured up to $\sqrt{s} = 1.8$ TeV at the Tevatron [3–8]. Both the values of the cross sections and the difference between pp and $p\bar{p}$ affect phenomenological models [9–14].

2. The experiment

The results presented here were obtained by the STAR experiment [15] upgraded with the Roman Pot (RP) system used previously by the PP2PP experiment [16]. The current RP system was installed downstream of the STAR main detector at RHIC and was used to detect forward-scattered protons. A modification of the vacuum chamber was required and the RP system was fully integrated with the STAR experiment. With the addition of the RP system, the STAR physics program now includes pp elastic scattering and two other measurements that require the detection of forward protons: Central Exclusive Production [17] and particle production in both Single Diffraction Dissociation and Central Diffraction [18]. In these inelastic events, the components of the main part of the STAR detector are used to characterize the recoil system at central rapidity.

The location of the RPs, top and side view, and the four Si detectors and a trigger scintillation counter package in each of the RPs are shown schematically in Fig. 1. The four planes of Si strip detectors [16] with a pitch of 100 μm, two measuring the x-coordinate (X planes) and two measuring the y-coordinate (Y planes), were used to reconstruct the position of the proton at the RP. The scintillation counter in each RP was used for triggering on candidate events with forward protons. It was read by two photomultiplier tubes (PMTs) for redundancy and high trigger efficiency. The trigger required at least one valid signal in at least one out of eight possible PMTs on each side of the interaction point (IP).

The location between DX and D0 RHIC dipole magnets is such that no special accelerator conditions such as large β^* (the value of the betatron function at the IP) and parallel-to-point focusing, were needed to operate the RPs together with the rest of the STAR experiment's physics program.

The DX magnet and the detectors in the two RPs allow the measurement of the momentum vector of the scattered protons at the detection point. Using the known bending angle of the DX magnet, one can determine the scattering angle in the x, z plane, θ_x. Because of the symmetry of the RHIC rings, the field in the DX magnets on both sides of the IP are identical at the 10^{-3} level. Hence, the bending angles of the magnets are also the same. The scattering angle in the y, z plane, θ_y, is determined from the y-coordinate measured in the RPs. Consequently, the local angles at the RPs θ_x, θ_y are the same as the scattering angles at the IP.

The data were acquired with normal $\beta^* = 0.85$ m and were taken during the last four hours of an eight-hour store during the pp run in 2015. The last four hours were chosen to have beams
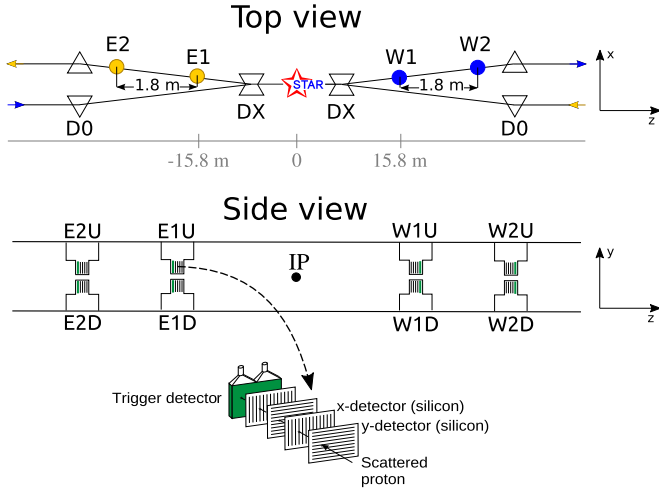
Fig. 1. The layout of the experiment. The four Roman Pot stations (E1, E2) on the East side of STAR and (W1, W2) on the West side of STAR are shown. In the upper panel, the view in the x, z plane is shown. In the lower panel, the y, z view is shown with the detector package, which includes four Si strip detector planes and the trigger scintillation counter. Two dipole magnets DX and D0, which bend the beams into and out of the IP, are also shown.

with reduced tails, thus with lower singles rates and background in the RP trigger counters. Three special luminosity measurements using Van der Meer scans [19] were performed to determine the luminosity and to reduce the systematic uncertainty on the luminosity measurement. The RPs were moved as close to the beam as possible, to about $8\sigma_y$ of the beam size in the y-coordinate, which was closer than during nominal data taking. The average instantaneous luminosity was $\approx 45 \cdot 10^{30}$ cm^{-2}s^{-1}. For this luminosity, the number of interactions per bunch crossing was 0.225 on average. Hence, pileup is not a concern.

There were about 6.7 million triggered events collected for the integrated luminosity of 1.8 pb^{-1}. The closest position of the first readout strip was about 30 mm or about $10\sigma_y$ of the beam, which corresponds to a minimum $|t|$ of about 0.03 GeV^2. The aperture of the DX magnet sets a maximum achievable limit of $|t| \approx 0.16$ GeV^2, corresponding to a scattering angle of $\theta \approx 4$ mrad.

3. Alignment and track reconstruction

Track reconstruction in the Si detectors was a three-step process: clustering that is used to determine the position of the proton trajectory in the Si plane, alignment to obtain the position of the proton in the elastic scattering coordinate system (the coordinate system in which two protons are collinear); and the reconstruction of a track, which leads to the reconstruction of the scattering angle needed to determine the t-value.

3.1. Clustering

To reconstruct track points in the RPs, we start with a clustering procedure for each Si detector plane separately. In the first step, the noise cut that selects energies greater than $3\sigma_{RMS}$ above the pedestal is applied for each strip. Then the clustering procedure searches for the channel with the maximum signal and a continuous series of channels adjacent to it. This cluster is then removed from the pool of hits in a given plane, and the procedure is repeated until there are no more hits in the plane. The position of the cluster is calculated as an energy-weighted average of the strip positions and their energies. The energy distribution of reconstructed clusters is well described by the convolution of Landau and Gauss distributions.

To reconstruct the x-coordinate the positions of clusters found in both X planes were compared. Given the limit on the maximum scattering angle of 4 mrad (Sec. 2) and the distance $\Delta z = 14$ mm between two X planes, a pair of clusters was accepted to calculate the x-coordinate if their position difference Δx satisfied condition that $\Delta x \leq 2 \cdot d_{strip} \approx 200$ μm, where d$_{strip}$ is the strip pitch. The x-coordinate of the track was calculated as an average of the matched cluster positions. The same procedure was done for y-coordinate using Y planes. Positions of pairs of matched clusters found in the detector planes measuring the same coordinate define x, y coordinates of space points for a given RP. In about 95% of events, only one reconstructed space point in an RP was found.

3.2. Alignment

Before the reconstruction of the scattering angle, an alignment procedure was performed in two steps, each producing one set of offsets. In the first step, survey data were utilized. That survey was done by the survey group of the accelerator department after the installation of the detector packages in the RPs. This survey determined the x, y position of the first strip in each detector package with respect to the accelerator coordinate system. In the second step, corrections to the survey alignment were obtained using reconstructed elastic events with the constraint of collinearity of elastic scattering for tracks reconstructed on each side of the IP. To make sure that the sample consisted of the cleanest elastic events, it was also required that these two point tracks were uniquely reconstructed (one and only one reconstructed point in each RP), providing two track points on each side of the IP.

For each event, a least squares line fit was done to the four reconstructed points. Then, the mean value of residuals for each detector plane, which was the average distance of reconstructed points from the fitted line, was calculated. Those mean residuals were used to correct the first strip position in each silicon detector plane, and the alignment process was then repeated with those new strip positions until residual distributions were centered at zero, giving the optimal relative positions between RPs on opposite sides of each detector arm separately. Typically three iterations were needed to obtain the offsets. The result of the second alignment step was a set of offsets in the coordinate system of the elastic scattering, where two outgoing protons are collinear. Those offsets were used to correct the positions of the Si strips from which the scattering angles θ_x, θ_y were reconstructed.

This alignment procedure was performed for each data run used in the analysis, and the mean value of run-by-run corrections was applied for each detector plane. By its construction, the alignment offsets were obtained in the system of coordinates where two protons are elastically scattered, hence collinear (elastic scattering geometry). Hence, the procedure left one variable unknown: the trajectory of the unscattered beam in the above coordinate system resulting from a beam-tilt angle in the collider, which affects the t-scale of the differential distribution dN/dt. The procedure to estimate the beam-tilt angle is described in section 5, where Monte Carlo (MC) corrections are described.

3.3. Scattering angle and t reconstruction

For small scattering angles θ, which are of the order of a few mrad, the positions of the track point x_{RP}, y_{RP} at a given RP station are given by:

$$x_{RP} = x_{IP} + \theta_x(z_{RP} - z_{IP}) \quad y_{RP} = y_{IP} + \theta_y(z_{RP} - z_{IP}) \quad (1)$$

where x_{IP}, y_{IP}, z_{IP} is the position of the primary vertex, z_{RP} is the surveyed z-position of the RP station, and θ_x, θ_y are the scattering angles. Since the position of the primary vertex is not known on an

event-by-event basis, two reconstructed points are required to calculate the scattering angle. A track was defined by the two points reconstructed in the two detector stations on the same side of the IP. The scattering angles θ_x and θ_y were determined by fitting a straight line using events with four track points, two on each side of the IP. Given the beam momentum p and small scattering angles θ_x and θ_y, the t-value was calculated using:

$$-t = (p_{in} - p_{out})^2 = p^2\theta^2 = p^2 \cdot (\theta_x^2 + \theta_y^2). \tag{2}$$

The resolution in t, Δt, is dominated by the beam angular divergence, as given by the machine emittance and by the beta value at the collision point ($\beta*$), and to a much lesser extent by the detector resolution. Thus, $\Delta t/t$ can be approximated by the term due to the beam angular divergence. For p = 100 GeV and $\delta\theta$ = 175 µrad and taking into account averaging over the two beams the $\Delta t/t$ is given by:

$$\frac{\Delta t}{t} = \sqrt{2}p\delta\theta/\sqrt{|t|} = 2.47 \times 10^{-2} \text{ GeV}/\sqrt{|t|}. \tag{3}$$

4. Data analysis

Because of the inclusive trigger condition, the collected data sample included the contributions from background, which consisted mostly of non-elastic events, elastic protons scattered on the apertures and accidental coincidences of the beam halo. The basic feature of the elastic scattering is that the two outgoing protons are back to back. This is called a collinearity condition, which is used as a main selection criterion of elastic events. The following cuts were used to select clean elastic events from the collected data sample:

1. **Elastic event topology (ET)**: Only events with a combination of reconstructed points in the RPs consistent with elastic scattering were accepted. Namely, the combinations with the lower East detector in coincidence with the upper West detector (EDWU), or the upper East detector in coincidence with the lower West detector (EUWD) have by definition the elastic event-hit pattern due to momentum conservation. In Fig. 2, we show the collinearity condition $\Delta\theta_y$ vs $\Delta\theta_x$, where $\Delta\theta_x = \theta_x^W - \theta_x^E$ and $\Delta\theta_y = \theta_y^W - \theta_y^E$. Here, the $\theta_x^W, \theta_x^E, \theta_y^W, \theta_y^E$ are scattering angles reconstructed on the East and West sides of the IP, using the coordinates measured at the RP and the average IP position. The contours of $2\sigma_\theta$ and $3\sigma_\theta$ are also shown. A clear peak of elastic events is seen.

2. **4-point track (4PT) data sample**: Only events with two-point tracks on the East and two-point tracks on the West (one track point in each RP in elastic combination) were kept.

3. **Collinear (COL) events**: Since elastic events must satisfy a collinearity condition, collinearity in θ^W, θ^E was required. Here, the θ^W, θ^E are reconstructed scattering angles on the West and East sides of the IP. Since $\Delta\theta = \theta_W - \theta_E = 0$, collinearity within $2\sigma_\theta$ was required, namely $\Delta\theta < 2\sigma_\theta$, where $\sigma_\theta = 244$ µrad is the Gaussian width of the collinearity distribution, consistent with the beam angular divergence. The collinearity condition required also the radial distance between the two projected tracks in x and y at $z = 0$ to be within 5σ radius of the Gaussian width of its radial distance. The $2\sigma_\theta$ cut was chosen to minimize background as described in Sec. 5.

4. **Fiducial volume GEO cut**: After the elastic event candidates were chosen based on collinearity, one more set of cuts in a fiducial volume ($\phi, |t|$), where ϕ is the azimuthal angle of the scattered proton, was needed to remove the remaining background. To stay away from the beam halo, the minimum $|t|$
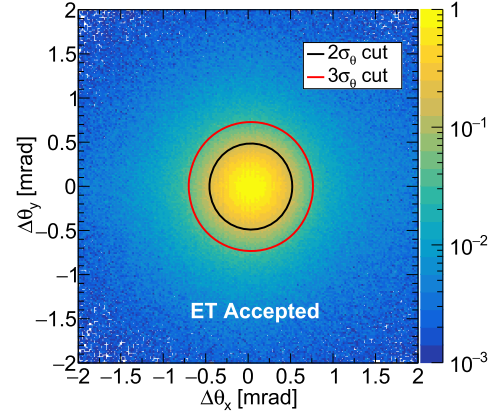

Fig. 2. Collinearity of the data sample $\Delta\theta_y$ vs $\Delta\theta_x$ for ET accepted events is shown. It is defined as the differences $\Delta\theta_x$ and $\Delta\theta_y$ between scattering angles θ_x, θ_y reconstructed on the East and West side of the IP. It is plotted with the contours of $2\sigma_\theta$ and $3\sigma_\theta$, where $\sigma_\theta = 244$ µrad.
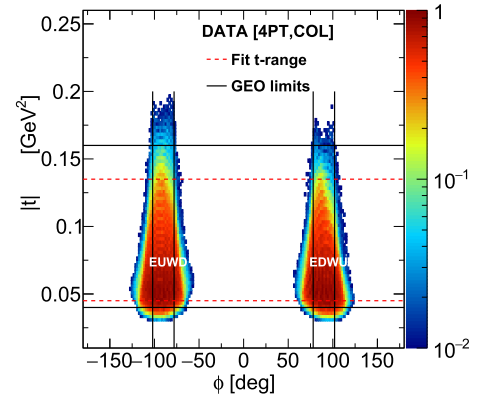

Fig. 3. Four-momentum transfer $|t|$ vs ϕ distributions for data for four-point collinear (4PT COL) events. The two elastic combinations of tracks between East and West, EUWD and EDWU, are shown. Each distribution is normalized to 1.

corresponding to 12σ of the beam size was required; this was well outside of the beam envelope. Hence, the coincidence of the beam halo from the two beams is not expected.

To stay away from the apertures, additional cuts on maximum $|t|$ and ϕ-range in ($\phi, |t|$) space were also required. They are shown in Fig. 3, where the lines labeled "GEO limits" show the limits of the geometrical acceptance and the fit range in ($\phi, |t|$) space accordingly. These cuts were chosen based on the simulation, which is described in Sec. 5. They were $78 < |\phi| < 102$ deg and $0.045 \leq -t \leq 0.135$ GeV^2.

We started with 6.607M events. After the ET cut there were 3.974M events left, 1.648M after the 4PT cut and 1.306M after the collinearity COL cut. The final sample had 0.666M events after the fiducial GEO cut.

5. Simulation and correction factors

Response of the detector was studied using a Monte Carlo data sample (G4MC) obtained with a GEANT4-based [20] software package. The simulation had a detailed implementation of the beam line and RP detector position, and of the Si detector readout behavior, where the point-reconstruction efficiency in each RP was determined from the data. The physics generator used for the simulation produced only elastic pp scattering at $\sqrt{s} = 200$ GeV, as described by Eq. (7), namely $dN/dt \propto \exp(-B|t|)$ with $B = 14$ GeV^{-2} and uniform distribution in ϕ. The kinematic range was
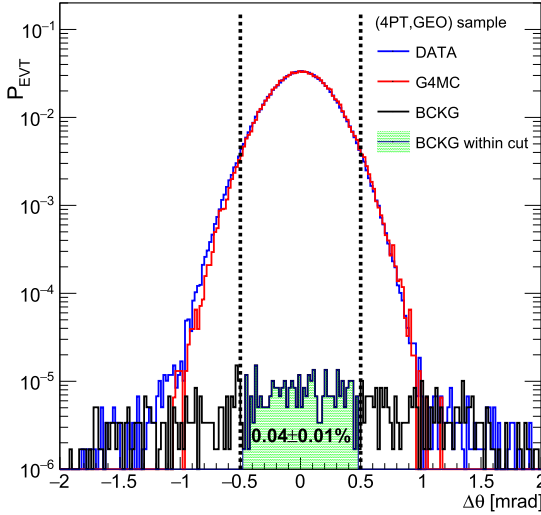
Fig. 4. Collinearity, $\Delta\theta = \theta^W - \theta^E$, for data is compared with prediction from the G4MC MC. Both samples were required to pass fiducial volume cuts (4PT, GEO). Estimated background (BCKG), and background remaining after the collinearity cut (green area), are also shown. The vertical axis is probability per event (P_{EVT}).

$-\pi \leq \phi \leq \pi$ and $0.01 \leq -t \leq 0.5$ GeV^2. The simulation was used to correct the measured dN/dt distributions from which the cross sections were obtained.

Using this simulation, the efficiency corrections were obtained as a function of t:

$$\epsilon(t_{reco}) = \frac{(dN/dt)^{MC}_{gen}}{(dN/dt)^{MC}_{reco}} \qquad (4)$$

where $(dN/dt)^{MC}_{gen}$ and $(dN/dt)^{MC}_{reco}$ are the true and reconstructed distributions, respectively, based on a MC event sample which passed reconstruction and selection steps identical to those applied to the experimental data. The t_{reco} is the t-value calculated at the end of the MC reconstruction chain, using the same procedure as in the data analysis. The geometrical acceptance of the detector was the main contribution to the efficiency corrections.

The differential distribution $(dN/dt)^{DATA}$ obtained from data was corrected using a "bin-by-bin" method according to Eq. (5) with correction factors from Eq. (4):

$$\left(\frac{dN}{dt}\right)^{DATA}_{corr} = \left(\frac{dN}{dt}\right)^{DATA}_{reco} \times \epsilon(t_{reco}). \qquad (5)$$

Based on the MC simulation, the $(|t|, \phi)$ region of the acceptance for the $d\sigma/dt$ fit was chosen so that it had a slowly varying dependence on $|t|$, which is shown in Fig. 5.

Additional corrections that needed to be considered were due to a possible non-zero initial colliding-beam angle (beam-tilt angle) and to the x, y position of the beam at the IP in the coordinate system of reconstructed elastic events. Such a beam tilt affects the t-scale of the measurement. Note that the offset due to the x, y position of the beam at the IP, being a parallel shift, does not change the reconstructed scattering angles θ_x, θ_y, which are the result of fitting a straight line to the four-point events.

The beam-tilt angle causes offsets τ_x and τ_y of the reconstructed θ_x and θ_y angles. This leads to an offset in the calculated t-values, which in lowest order is given by:

$$\Delta t \simeq 2 \cdot p^2 \cdot (\theta_x \cdot \tau_x + \theta_y \cdot \tau_y). \qquad (6)$$

Since the efficiency correction function was obtained from an MC simulation with a beam trajectory parallel to the detector local coordinate z-axis, this beam-tilt angle needed to be accounted for in the MC simulated efficiency correction function.

To determine τ_x and τ_y the dN/dt distribution from the data, Fig. 5 was used. The τ_x, τ_y angles were varied within $[-0.2, 0.3]$ mrad and fitted to the data looking for the best fit probability. That best χ^2 determined the beam crossing angles τ_x and τ_y to be 0.15 mrad and 0.015 mrad, respectively. Note that the τ_y is negligible compared to typical scattering angles of a few mrad. The contribution to the systematic uncertainties from the tilt angle was evaluated as described in Sec. 6.

A GEANT4-based simulation was also used to study protons interacting with material in front of the RPs such as the beam pipe, magnet structure and RF shield inside the DX-D0 chamber, etc. In Fig. 4, we compare the collinearity distributions for reconstructed data and reconstructed MC samples. We see a very good agreement between MC and the data. The vertical axis in Fig. 4 is the probability per event (P_{EVT}). An estimate of the background (bckg) contribution is also shown. It was obtained using unpaired protons in the whole elastic trigger data sample by flipping the sign of (x, y) coordinates of reconstructed points on one side of the IP. Then, the cuts of the analysis procedure were applied to all the events. This study is sensitive to the beam halo and to the inelastic events in our data sample. Consequently, it made it possible to estimate the total (see Fig. 4) and differential dN/dt background contribution. The latter was subtracted from the final $d\sigma/dt$, to estimate impact of the background on the fit results. We found small changes of B-slope and $d\sigma_{el}/dt|_{t=0}$, 0.006 GeV^{-2} and -0.006 mb/GeV^2 respectively. These values were added in quadrature to the total systematic uncertainty. But given the number of significant digits, they did not change the result in Table 1.

Also, since the beam momentum uncertainty was at the 10^{-3} level, it was neglected. The RP point reconstruction efficiency implemented in the MC simulation was obtained from the data. The trigger efficiency determined from the data was essentially 100%, so no corrections were made.

6. Results

Over the t-range of this measurement $0.045 \leq -t \leq 0.135$ GeV^2, the differential cross section $d\sigma/dt$ is dominated by the hadronic term, whose t-dependance is well described by an exponential with one free slope parameter B and the normalization factor:

$$\frac{d\sigma^{had}_{el}}{dt} = \left.\frac{d\sigma^{had}_{el}}{dt}\right|_{t=0} \cdot e^{-B|t|} \qquad (7)$$

Hence, a two-parameter exponential fit was performed to the measured differential cross-section $d\sigma/dt$ to obtain the slope parameter B. We performed fitting using the bin center.

The total cross section was obtained using the optical theorem, given in Eq. (8), which relates the total cross section to the value of the hadronic elastic cross section at $t = 0$:

$$\sigma^2_{tot} = \left(\frac{16\pi(\hbar c)^2}{1 + \rho^2}\right) \left.\frac{d\sigma^{had}_{el}}{dt}\right|_{t=0}. \qquad (8)$$

The ρ parameter in Eq. (8) is the ratio of the real to the imaginary part of the hadronic scattering amplitude and it was not measured in this experiment. Its value was obtained from a fit to the world data using the COMPETE [11] model, which is based on Regge theory [12,13]. Because $\rho = 0.12$ and enters Eq. (8) in quadrature, the uncertainty on ρ does not contribute significantly to the obtained value of σ_{tot}. For the ρ-uncertainty we varied its value by ± 0.05 and fitted Eq. (7) to get the estimate of the corresponding systematic uncertainty.

The fit of the Eq. (7) with its results is shown in Fig. 5. The bin size in the fitted histogram is 0.0025 GeV^2, which is smaller than the t-resolution. However, the fit was repeated with larger bin
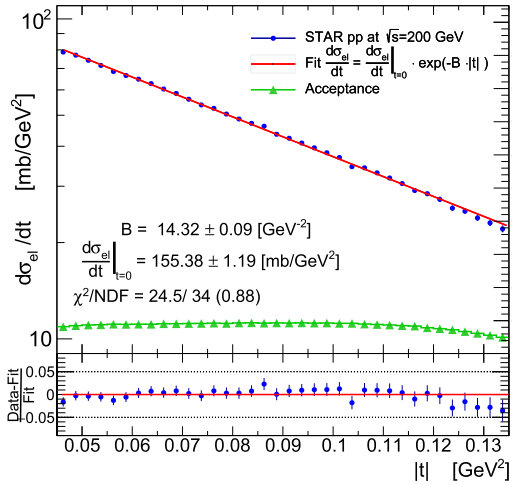
Fig. 5. Top panel: *pp* elastic differential cross-section $d\sigma/dt$ fitted with exponential $A \exp(Bt)$. The green triangles and the scale on the right-hand side of the plot show the MC simulated geometrical acceptance. Bottom panel: Residuals (Data - Fit)/Fit. Uncertainties are statistical only.

Fig. 6. Comparison of STAR result on *B*-slope with the world data with the *t*-range of this experiment. Below 1.8 TeV data are from [21], the Tevatron data are [3–5] and the LHC data are [1,23,24,26–28]. The *t*-range for the world data was chosen to be compatible with the STAR *t*-range.
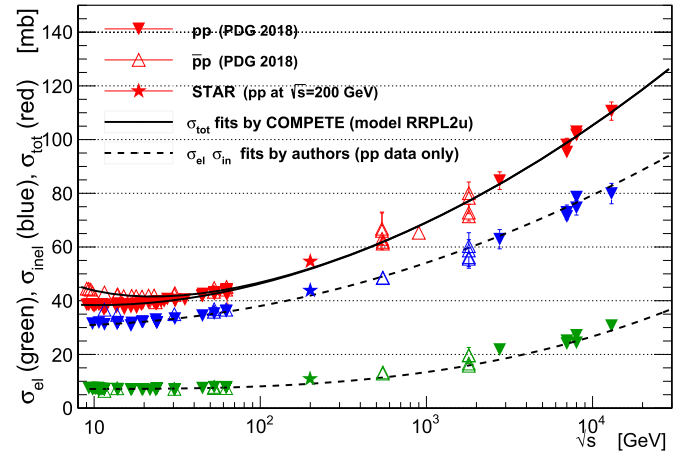
Fig. 7. Comparison of STAR results on σ_{tot}, σ_{inel} and σ_{el} with the world data for data below 1.8 TeV [22], the Tevatron [4–7] and the LHC experiments [1,23–25,27,28]. The COMPETE prediction for σ_{tot} is also shown. The dashed curves, represent STAR fits to σ_{inel} and σ_{el} using the same function as used by COMPETE. STAR data points were not used in the fit.

sizes by factor 2, 3 and 4 and also the MC based study of bin-to-bin migration showed that actual bin size does have a significant impact on the fit parameter values except to increase statistical uncertainties with decreasing NDF of the fit.

The dependence of the MC correction factors on the value of the initial slope *B* was also investigated. The initial MC *t*-distributions were reweighed with the slope from the reconstructed data at detector level $B_{det} = 14.8$ GeV^{-2}, and the correction factors were recalculated. The fit results to *B* and to $d\sigma_{el}/dt|_{t=0}$ changed by 0.01 GeV^{-2} and 0.01 mb/GeV^2 respectively. Since they did not change the total systematic uncertainty within accuracy displayed in Table 1, they are not listed in there.
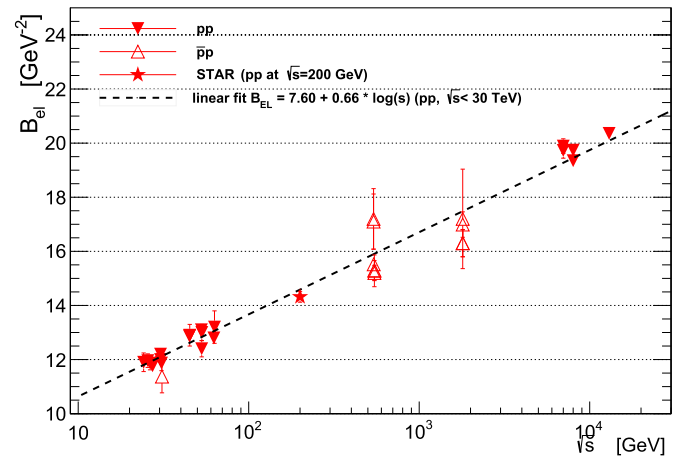
The evaluation of the uncertainties due to the beam angular divergence, the vertex positions and their spread, and incoming beam angles was based on MC simulations described in the previous section. We found that the largest single source of the systematic error of the *t*-scale of the experiment was due to the beam-tilt angle. This shift of the *t*-distribution scale was studied with the MC simulation using the upper limits on the beam-tilt angle obtained from data. It resulted in an uncertainty on the fitted slope parameter of about 2%.

We observe a weak dependence of the fitted slope *B* and σ_{tot} on the values of the beam-tilt angles, which were accounted for in a contribution to the systematic uncertainties.

For the cross section measurements, the largest systematic uncertainty is due to luminosity determination, which was estimated to be 4%. This is the scale uncertainty on the vertical scale of the cross section plot. It introduces a corresponding systematic uncertainty to the cross sections listed in Table 1.

As described in Sec. 5, the estimated background contribution due to the particle interactions with the material in front of the RPs and within the geometrical acceptance used for this analysis was negligible, hence such a correction was not required.

Table 1 contains our final results and uncertainty estimates with the six observables listed in the left column. They are: the intercept of the differential cross section $d\sigma_{el}/dt|_{t=0}$; the slope parameter *B*; the total cross section σ_{tot} obtained using optical theorem; the elastic cross section σ_{el}, which was obtained by simply integrating the fitted exponential over all *t*; the elastic cross section integrated within the STAR *t*-range σ_{el}^{det}; and the inelastic cross section σ_{inel}, which was obtained by subtracting σ_{el} from σ_{tot}. As such, both σ_{el} and σ_{inel} are estimates. Nevertheless, we see good agreement with the world data. This is because most

of the σ_{el} is in the purely exponential region measured in this experiment. The last column of Table 1 lists the total systematic uncertainty, which was obtained by adding the individual systematic uncertainties in quadrature. The ρ-parameter column in the table lists the systematic uncertainty due to the uncertainty in the ratio of the real to the imaginary part of the hadronic scattering amplitude.

The asymmetric systematic uncertainties on the cross sections are due to the luminosity uncertainty, which is the dominant uncertainty of the measurement.

The comparison of our results with the world data on the nuclear slope parameter *B* is shown in Fig. 6, and on σ_{tot}, σ_{inel}, σ_{el} are shown in Fig. 7, where the total uncertainty of the STAR data points was obtained by adding the statistical and systematic uncertainties in quadrature. STAR results agree well with the world data and with the COMPETE model [11], which is a fit to the existing world data available prior to this measurement and which is now commonly used as a reference comparison with the data.

Table 1
Results summary with systematic uncertainties.

Quantity			Statistical	Systematic uncertainties			
Name	Units	Value	Uncertainty	Beam tilt	Luminosity	ρ-parameter	Total sys.
$d\sigma_{el}/dt\|_{t=0}$	[mb/GeV^2]	155.38	±1.19	$^{+1.19}_{-0.91}$	$^{+7.05}_{-6.47}$	–	$^{+7.15}_{-6.53}$
B	[GeV^{-2}]	14.32	±0.09	$^{+0.13}_{-0.28}$	–	–	$^{+0.13}_{-0.28}$
σ_{tot}	[mb]	54.67	±0.21	$^{+0.21}_{-0.64}$	$^{+1.23}_{-1.15}$	$^{+0.27}_{-0.41}$	$^{+1.28}_{-1.38}$
σ_{el}	[mb]	10.85	±0.03	$^{+0.07}_{-0.04}$	$^{+0.49}_{-0.41}$	–	$^{+0.49}_{-0.41}$
σ_{el}^{det}	[mb]	4.05	±0.01	$^{+0.02}_{-0.01}$	$^{+0.18}_{-0.17}$	–	$^{+0.18}_{-0.17}$
σ_{inel}	[mb]	43.82	±0.21	$^{+0.22}_{-0.64}$	$^{+1.32}_{-1.22}$	$^{+0.27}_{-0.41}$	$^{+1.37}_{-1.44}$

7. Summary

The STAR experiment measured the elastic differential cross-section in pp scattering as a function of t in the range $0.045 \leq -t \leq 0.135$ GeV^2 at $\sqrt{s} = 200$ GeV. This cross-section is well described by $e^{-B|t|}$ with the slope $B = 14.32 \pm 0.09(stat.)^{+0.13}_{-0.28}(syst.)$ GeV^{-2}. The total pp cross-section was found to be $\sigma_{tot} = 54.67 \pm 0.21(stat.)^{+1.28}_{-1.38}(syst.)$ mb. Extrapolation of the measured differential elastic cross-section to the outside of the STAR t-acceptance permitted the determination of $\sigma_{el} = 10.85 \pm 0.03(stat.)^{+0.49}_{-0.41}(syst.)$ mb. We also determined the elastic cross section integrated within the STAR t-range $\sigma_{el}^{det} = 4.05 \pm 0.01(stat.)^{+0.18}_{-0.17}(syst.)$ mb. By subtracting the calculated σ_{el} from σ_{tot}, we also obtained an inelastic cross section $\sigma_{inel} = 43.82 \pm 0.21(stat.)^{+1.37}_{-1.44}(syst.)$ mb. We find that the obtained results are in good agreement with the world data. The σ_{tot} agrees with the COMPETE prediction at $\sqrt{s} = 200$ GeV of 51.79 mb within about 2σ of the total uncertainty.

Declaration of competing interest

The authors declare that they have no known competing financial interests or personal relationships that could have appeared to influence the work reported in this paper.

Acknowledgements

References

[1] G. Antchev, et al., TOTEM Collaboration, and references therein, Eur. Phys. J. C 79 (2019) 103.
[2] U. Amaldi, et al., CERN-Pisa-Rome-Stony Brook Collaboration, Phys. Lett. B 62 (1976) 460.
[3] N.A. Amos, et al., E710 Collaboration, Phys. Rev. Lett. 61 (1988) 525.
[4] N.A. Amos, et al., E710 Collaboration, Phys. Rev. Lett. 63 (1989) 2784.
[5] N.A. Amos, et al., E710 Collaboration, Phys. Rev. Lett. 68 (1989) 2433.
[6] F. Abe, et al., CDF Collaboration, Phys. Rev. D 50 (1994) 5518.
[7] C. Avila, et al., E811 Collaboration, Phys. Lett. B 537 (2002) 41.
[8] V.M. Abazov, et al., D0 Collaboration, Phys. Rev. D 86 (2012) 012009.
[9] C. Bourrely, J. Soffer, T.T. Wu, Eur. Phys. J. C 28 (2003) 97.
[10] B.Z. Kopeliovich, I.K. Potashnikova, B. Povh, Phys. Rev. D 86 (2012) 051502.
[11] J.R. Cudell, et al., COMPETE Collaboration, Phys. Rev. Lett. 89 (2002) 201801.
[12] V. Barone, E. Predazzi, High-Energy Particle Diffraction, Texts and Monographs in Physics, Springer-Verlag, ISBN 3540421076, 2002.
[13] S. Donnachie, G. Dosch, P. Landshoff, Pomeron Physics and QCD, Cambridge University Press, ISBN 9780521675703, 1998.
[14] M.M. Block, et al., Phys. Rev. D 93 (2016) 114009.
[15] K.H. Ackermann, et al., STAR detector overview, Nucl. Instrum. Methods, Sect. A 499 (2003) 624.
[16] S. Bultmann, et al., PP2PP Collaboration, Nucl. Instrum. Methods, Sect. A 535 (2004) 415.
[17] R. Sikora, STAR Collaboration, Acta Phys. Pol. B, Proc. Suppl. 12 (2019) 811.
[18] L. Fulek, STAR Collaboration, Acta Phys. Pol. B, Proc. Suppl. 12 (2019) 999.
[19] S. Van Der Meer, ISR-PO/68-31, KEK68-64.
[20] S. Agostinelli, et al., Nucl. Instrum. Methods, Sect. A 506 (2003) 250, http://geant4.web.cern.ch/geant4.
[21] HEP Durham Data base, http://hepdata.cedar.ac.uk/review/pp2/.
[22] M. Tanabashi, et al., Particle Data Group, Phys. Rev. D 98 (2018) 030001, http://pdg.lbl.gov/2018/hadronic-xsections/hadron.html.
[23] G. Antchev, et al., TOTEM collaboration, Europhys. Lett. 101 (2) (2013) 21004.
[24] G. Antchev, et al., TOTEM collaboration, Eur. Phys. J. C 76 (2016) 661.
[25] F.J. Nemes, TOTEM Collaboration, PoS DIS2017 (2017) 059.
[26] G. Antchev, et al., TOTEM collaboration, Eur. Phys. J. C 80 (2020) 91.
[27] G. Aad, et al., ATLAS collaboration, Nucl. Phys. B 889 (2014) 486.
[28] M. Aaboud, et al., ATLAS collaboration, Phys. Lett. B 761 (2016) 158.